Available online at www.sciencedirect.com
ScienceDirect
Trans. Nonferrous Met. Soc. China 34(2024) 3762−3776
Transactions of Nonferrous Metals Society of China
www.tnmsc.cn

Effects of Ti- and Mg-bearing minerals on hydrothermal formation of hydroandradite

Hong-fei WU[1,2,3], Xiao-lin PAN[1,2,3], Ying-jie HE[2], Hai-yan YU[1,2,3]

1. Key Laboratory for Ecological Metallurgy of Multimetallic Mineral of Ministry of Education, Northeastern University, Shenyang 110819, China;
2. School of Metallurgy, Northeastern University, Shenyang 110819, China;
3. Key Laboratory for Recycling of Nonferrous Metal Resources (Shenyang), Shenyang 110819, China

Received 2 June 2023; accepted 26 February 2024

Abstract: The effects of Ti- and Mg-bearing minerals on the crystal structure, morphology, particle size distribution, and formation mechanism of efficient desilication product of hydroandradite (HA) during hydrothermal conversion in a synthetic sodium aluminate solution were investigated via X-ray diffractometer, scanning electron microscope and particle size analyzer. During HA formation, anatase, rutile, and periclase dissolved in sodium aluminate solution engage in ion substitution reactions between Ti^{4+} and Si^{4+}, and between Mg^{2+} and Ca^{2+}, respectively. However, dissolved hydromagnesite cannot enter into the HA. The content of HA after the hydrothermal reactions changes slightly with the increase of anatase and periclase contents, but it notably decreases with increased quantities of rutile and hydromagnesite. Ti-bearing minerals reduce the particle size and enhance the specific surface area of HA, whereas Mg-bearing minerals exert the opposite effect. The morphology of HA with Ti- and Mg-bearing minerals changes from spherical particles to flocculent structure and hexagonal plate-like particles.

Key words: hydroandradite; anatase; rutile; periclase; hydromagnesite; desilication; hydrothermal conversion

1 Introduction

During the alumina production through the Bayer process, Ti- and Mg-bearing minerals present in bauxites, and additives not only significantly impair alumina digestion performance, but also cause damage to digestion pipes, reducing heat exchange efficiency and increasing production costs [1]. The bauxites usually contain 2%−8% of Ti-bearing minerals in the forms of anatase, rutile, and brookite [2,3]. The MgO contained in lime additive (1%−5%) and bauxites (<1%) is the main source of Mg-bearing minerals [4]. The effects of Ti- and Mg-bearing minerals on alumina extraction, desilication reactions and scab formation in the $CaO−Na_2O−Al_2O_3−SiO_2−H_2O$ system were widely studied [5−7].

The Ti-bearing minerals can react with the caustic solution during alumina extraction, forming a dense protective film layer of sodium titanate on the bauxite surface, hindering subsequent liquid−solid reactions. Notably, the binding capacity of Ti-bearing minerals with the caustic solution decreases in the sequence of amorphous titanium oxide, anatase, brookite, and rutile [1,8]. To eliminate the inhibition effects of Ti-bearing minerals, an appropriate amount of lime is typically added to the original slurry during high-pressure digestion process to enhance the alumina extraction efficiency and reaction rate [9−12]. These minerals can react with Ca-bearing compounds to create calcium titanate

Corresponding author: Xiao-lin PAN, Tel: +86-24-83686460, E-mail: panxl@smm.neu.edu.cn
DOI: 10.1016/S1003-6326(24)66639-2

compounds, following the phase transformation sequence $TiO_2 \rightarrow Na_2TiO_3 \rightarrow CaO \cdot 2TiO_2 \cdot H_2O \rightarrow CaTiO_3$ [13,14]. The detitanization reactions exhibit an apparent activation energy of 84.4 kJ/mol at temperatures ranging from 180 to 260 °C during the digestion process, primarily controlled by surface chemical reactions [15,16]. However, the precipitation of calcium titanate on pipeline surfaces notably diminishes heat transfer efficiency, leading to potential blockages and increased energy consumption and production costs.

The presence of MgO in bauxites and lime additives can cause the formation of various Mg-bearing compounds at elevated temperatures in alkaline conditions, including $MgAl_2O_4$, $Mg(OH)_2$, $MgCO_3$, $Mg_6Al_2CO_3(OH)_{16} \cdot 4H_2O$, $NaCa_2Mg_5Si_7AlO_{22}$, and $Mg_2Al_4Si_9O_{13}$ [17,18]. During the heating process of bauxite slurry, Mg-bearing minerals are primarily found in the forms of $Mg(OH)_2$ and magnesium aluminosilicate hydrate (MAH, $Mg_{6-x}(Al_xSi_{4-x})O_{10} \cdot (OH)_8$), with MgO content in scabs on the digestion pipeline reaching 4% to 11% [19]. In the desilication process under atmospheric pressure, MgO readily combines with sodium aluminate solution upon lime addition to form silicate ($(Mg_4Al)(SiAlO_5)(OH)_4$), thereby improving the desilication efficiency but leading to the loss of alumina [5]. Additionally, compounds of hydrogarnet (HG, $3CaO \cdot Al_2O_3 \cdot xSiO_2 \cdot (6-2x)H_2O$), $Mg_{6-x}(Al_xSi_{4-x})O_{10} \cdot (OH)_8$, and sodium aluminosilicate hydrate (SAH, $Na_8[Al_6Si_6O_{24}] \cdot X_2 \cdot nH_2O$) can form during high-temperature desilication processes [20]. Thermodynamics calculation has indicated that MgO has a more substantial influence on the formation of HG than on the formation of SAH [5,21].

Based on the aforementioned research, Ti- and Mg-bearing minerals significantly influence the formation of traditional desilication products (DSPs) in the $CaO-Na_2O-Al_2O_3-SiO_2-H_2O$ system. Recent studies have focused on the hydrothermal formation and transformation of hydroandradite (HA, $3CaO \cdot Fe_2O_3 \cdot xSiO_2 \cdot (6-2x)H_2O$) in the $Fe_2O_3-Na_2O-Al_2O_3-CaO-SiO_2-H_2O$ system, as an efficient DSP theoretically devoid of alkali and alumina [22]. HA represents an ideal target DSP for processing low-grade bauxites and Bayer red mud. However, the impact of Ti- and Mg-bearing minerals on the formation and transformation of HA remains unclear. This work aimed to reveal the formation process and reaction mechanism of HA with different Ti- and Mg-bearing minerals in a synthetic sodium aluminate solution. The lattice parameters, particle size, phase composition, and morphology of HA during the hydrothermal conversion were systematically investigated, which can provide a theoretical guidance for the formation regulation of HA as well as the reduction of red mud.

2 Experimental

2.1 Materials

The sodium aluminate solution used in the experiments was prepared by dissolving $NaAlO_2$, $Na_2SiO_3 \cdot 9H_2O$ and NaOH solution. All materials utilized in the hydrothermal process were analytical reagents. The concentration of the synthetic sodium aluminate solution was listed as follows: the caustic alkali concentration (in the form of Na_2O) was 240 g/L, the molar ratio of Na_2O to Al_2O_3 was 20, and the silica concentration was 10 g/L. The calcium oxide (CaO) was obtained by calcining $CaCO_3$ at 1100 °C for 2 h. The sodium ferrite ($NaFeO_2$) was synthesized by roasting at 950 °C for 1.5 h employing Fe_2O_3 and Na_2CO_3 at the identical molar ratio. The mixture of reactants was performed at the molar ratio of $CaO:Fe_2O_3:SiO_2$ being 3:1:1. The Ti-bearing minerals used were rutile (TiO_2) and anatase (TiO_2), while the Mg-bearing minerals included hydromagnesite ($Mg_5(CO_3)_4(OH)_2 \cdot 4H_2O$) and periclase (MgO), with concentrations ranging from 2.5 to 10 g/L. The XRD patterns of the Ti- and Mg-bearing minerals are illustrated in Fig. 1, demonstrating that the characteristic peaks of these minerals closely match with the standard cards.

2.2 Methods

The hydrothermal reactions were completed in a series of 150 mL bomb reactors, rotating at 45 r/min and heated using nitrate molten salts in a high-pressure group autoclave. The hydrothermal reaction temperature and reaction time were 260 °C and 60 min, respectively. The contents of Na_2O and Al_2O_3 in sodium aluminate solution were tested by the acid−base neutralization titration method and EDTA titration method, respectively. The concentration of SiO_2 was analyzed via the molybdenum blue photometric method. The relative intensity ratio (RIR) method was employed to semi-quantitatively analyze the mass fractions of each

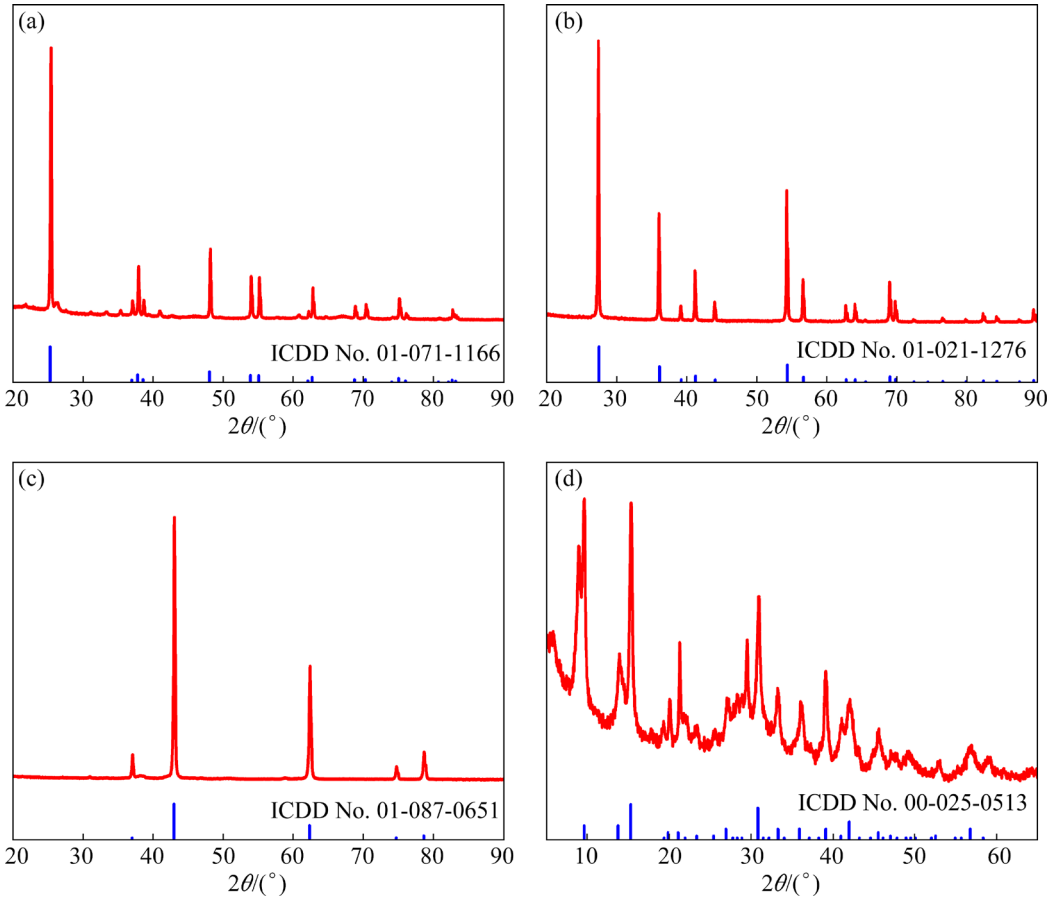

Fig. 1 XRD patterns of Ti- and Mg-bearing minerals: (a) Anatase; (b) Rutile; (c) Periclase; (d) Hydromagnesite

crystalline phase (w_i) in the reaction products as depicted in Eq. (1) [23]. The crystallinity and lattice parameters of the reaction products were examined using the Jade software. Initially, the XRD patterns of the reaction products were smoothened, and the characteristic peak intensities of crystalline and amorphous phases were accurately fitted. Subsequently, the crystallinity of the reaction products was determined by dividing the intensities of crystal phase to the total intensities.

$$w_i = \frac{I_i/\mathrm{RIR}_i}{\sum_{i=1}^{N}(I_i/\mathrm{RIR}_i)} \quad (1)$$

where I_i and RIR_i represent the strongest peak intensity and the reference intensity of phase i, respectively.

The compositions and structural characteristics of minerals were analyzed using an X-ray diffractometer (XRD, D8 Advance, Bruker, USA) with Cu $K_{\alpha 1}$ radiation, covering corresponding diffraction angles in the 2θ range from 5° to 90°. The microstructure of minerals was observed via a scanning electron microscope (SEM, JSM−6700F), while the distribution of element and mineral composition were assessed using an energy dispersive spectrometer (EDS, Xplore 30). The particle size distribution of reaction products was determined using a laser diffraction particle size analyzer (PSD, Malvern Mastersizer 3000).

3 Results and discussion

3.1 Effect of Ti- and Mg-bearing minerals on crystal structure

The compositions and properties of sodium aluminate solution serve as a crucial theoretical foundation for HA formation. The effects of Ti- and Mg-bearing minerals on the concentrations of sodium aluminate solution after the hydrothermal process were investigated, as displayed in Fig. 2. The concentrations of Na_2O and Al_2O_3 exhibit slight variations with the concentration of Ti-bearing minerals (Fig. 2(a)). However, as shown in Fig. 2(b), the Na_2O concentrations decrease with the increasing concentration of Mg-bearing minerals,

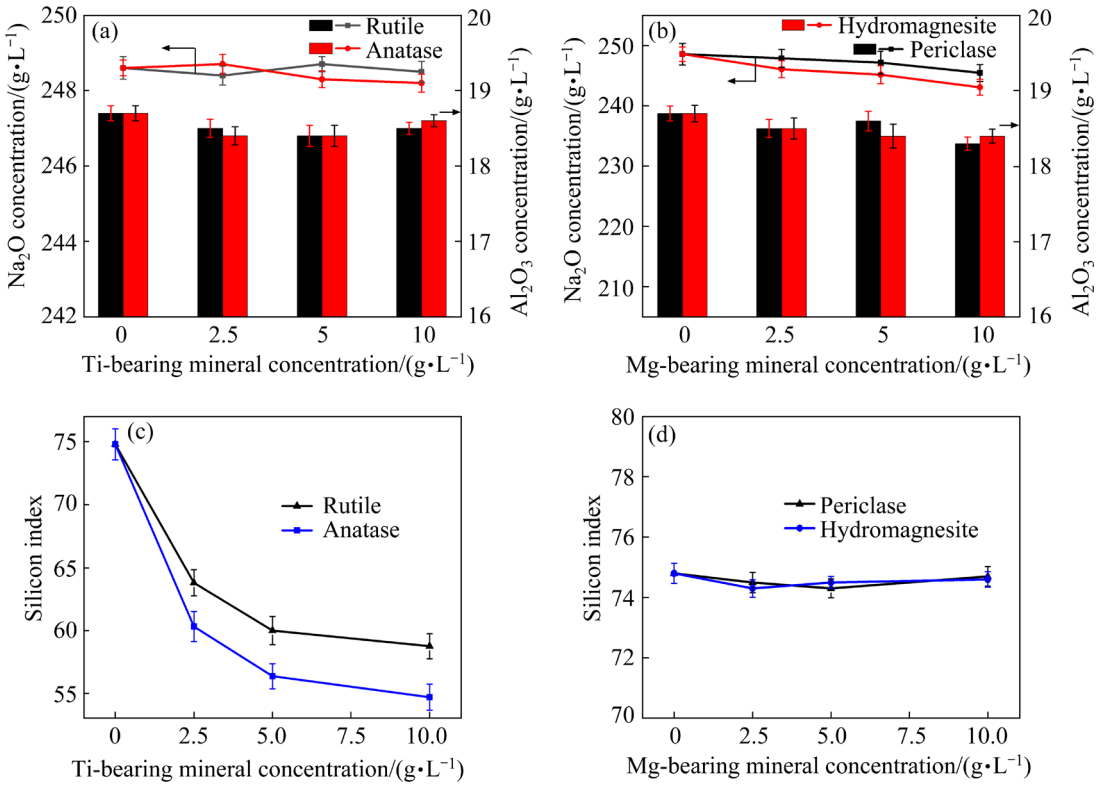

Fig. 2 Concentration change of sodium aluminate solutions with different Ti- and Mg-bearing minerals after hydrothermal process: (a, b) Na_2O and Al_2O_3 concentrations; (c, d) Silicon index

while the Al_2O_3 concentrations are almost the same. Additionally, the Na_2O concentrations in sodium aluminate solution with periclase are higher compared to those with hydromagnesite. This difference arises because hydromagnesite readily reacts with sodium aluminate solution, forming magnesium hydroxide, thereby reducing the Na_2O concentrations. As illustrated in Fig. 2(c), the silicon index of sodium aluminate solution decreases notably with increased levels of Ti-bearing minerals. This reduction occurs due to the substitution of the Si^{4+} in HA by the dissolved Ti^{4+}, which leads to the decrease of silicon index. Moreover, rutile dissolved in sodium aluminate solution is easier to substitute the Si^{4+} in HA compared to anatase. As shown in Fig. 2(d), the silicon index of sodium aluminate solution changes slightly with the concentration variation of Mg-bearing minerals, demonstrating that the Mg-bearing minerals have little effect on the silica concentrations.

The reaction behavior of Ti- and Mg-bearing minerals in sodium aluminate solution in the Fe_2O_3−Na_2O−Al_2O_3−CaO−SiO_2−H_2O system was investigated, and the corresponding XRD patterns of the reaction products are displayed in Fig. 3. The phases predominantly formed with anatase consist of HA ($3CaO·0.87Fe_2O_3·0.13Al_2O_3·1.65SiO_2·2.7H_2O$) and HG ($3CaO·Al_2O_3·SiO_2·4H_2O$), as shown in Fig. 3(a). When the concentration of anatase surpasses 5 g/L, the new diffraction peaks of calcium titanate ($CaTiO_3$) emerge. This is due to the reaction between Ti-bearing minerals and CaO in sodium aluminate solution, forming calcium titanate. This finding aligns with the results of LI et al [3], and the specific reaction is denoted as Reaction (2). Calcium titanate, being the most stable phase in bauxite residue, serves as the primary component of scabs on the heat transfer surfaces in alumina refineries [13]. In Fig. 3(b), it can be seen that the calcium titanate emerges when the concentration of rutile exceeds 2.5 g/L, demonstrating that the rutile dissolved in sodium aluminate solution is easier to combine with calcium oxide to form calcium titanate compared to anatase. As viewed from Fig. 3(c), the main phases include HA and HG, and magnesium hydroxide ($Mg(OH)_2$) appears when the periclase concentration exceeds 2.5 g/L. Moreover, when the concentration of the hydromagnesite exceeds 2.5 g/L, the calcium

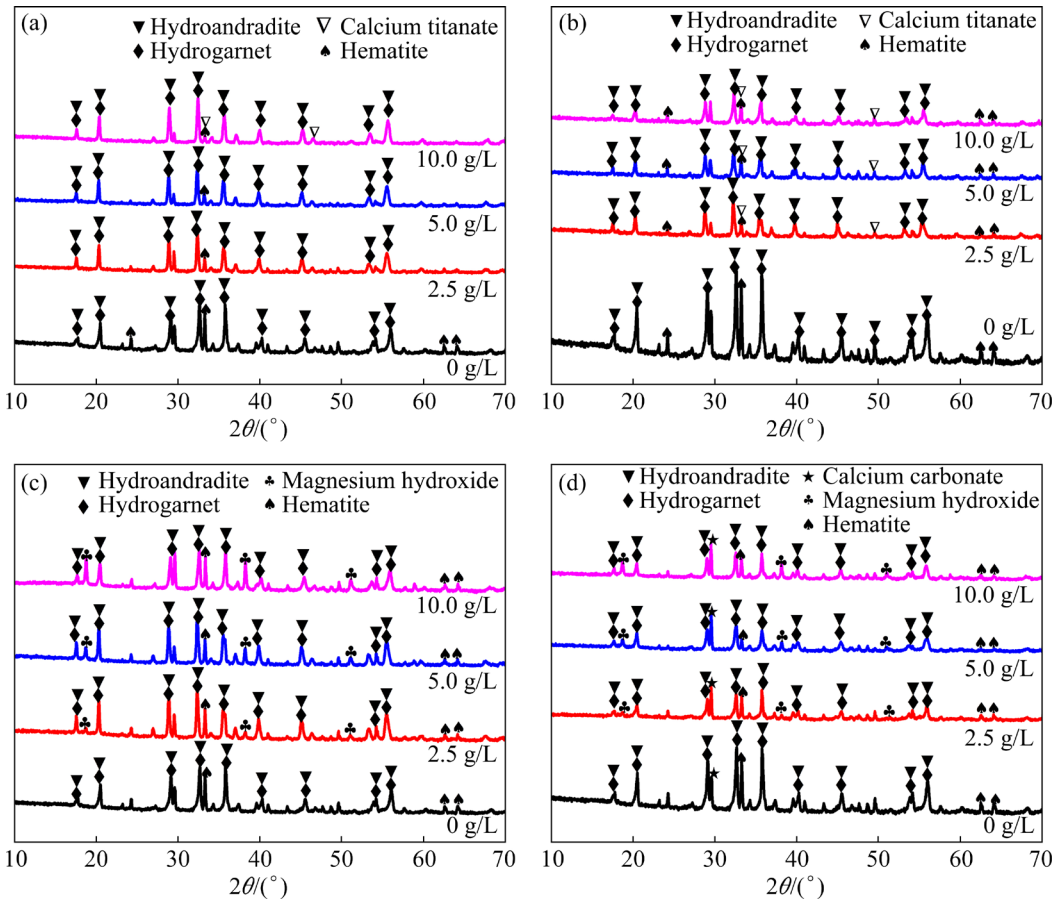

Fig. 3 XRD patterns of reaction products with different Ti- and Mg-bearing minerals: (a) Anatase; (b) Rutile; (c) Periclase; (d) Hydromagnesite

carbonate phase ($CaCO_3$) forms (Fig. 3(d)), and the main reaction occurring with hydromagnesite is illustrated in Reaction (3). Previous studies have indicated that the Mg-bearing minerals initially undergo hydration reactions in sodium aluminate solution, resulting in the formation of magnesium hydroxide, which then gradually dissolves [5]. Additionally, the solubility of magnesium hydroxide in sodium aluminate solution markedly decreases as the reaction temperature rises, becoming nearly insoluble at 178 °C [19].

$$TiO_2+Ca(OH)_2=CaTiO_3+H_2O \quad (2)$$

$$Mg_5(CO_3)_4(OH)_2\cdot 4H_2O+4Ca(OH)_2= 5Mg(OH)_2+4CaCO_3+4H_2O \quad (3)$$

The lattice parameters (a=b=c) and the crystallinity of HA with various Ti- and Mg-bearing minerals were computed based on the XRD patterns and presented in Fig. 4. It is evident from Figs. 4(a, b) that both the lattice parameters and crystallinity of HA decrease with an increase in the concentration of Ti-bearing minerals. The reason is that as the concentration of Ti-bearing minerals increases, the amount of dissolved Ti^{4+} entered into HA rises, which increases the degree of lattice distortion of HA. Figure 4(c) indicates that with an increase in the periclase concentration, the lattice parameters and crystallinity of HA decrease, implying that the periclase is harmful to the crystallization of HA. In Fig. 4(d), the lattice parameters of HA remain consistent despite an increase in hydromagnesite concentration, while the crystallinity of HA decreases. This is because the calcium carbonate generated by the reaction of hydromagnesite adheres to the surface of HA, which inhibits the nucleation and growth of HA. Therefore, both the Ti- and Mg-bearing minerals hinder HA formation, but the changes in lattice parameters and crystallinity of HA caused by Ti-bearing minerals are more significant than those caused by Mg-bearing minerals.

The contents (mass fraction) of HA with different Ti- and Mg-bearing minerals are illustrated in Fig. 5. The contents of HA and HG have little

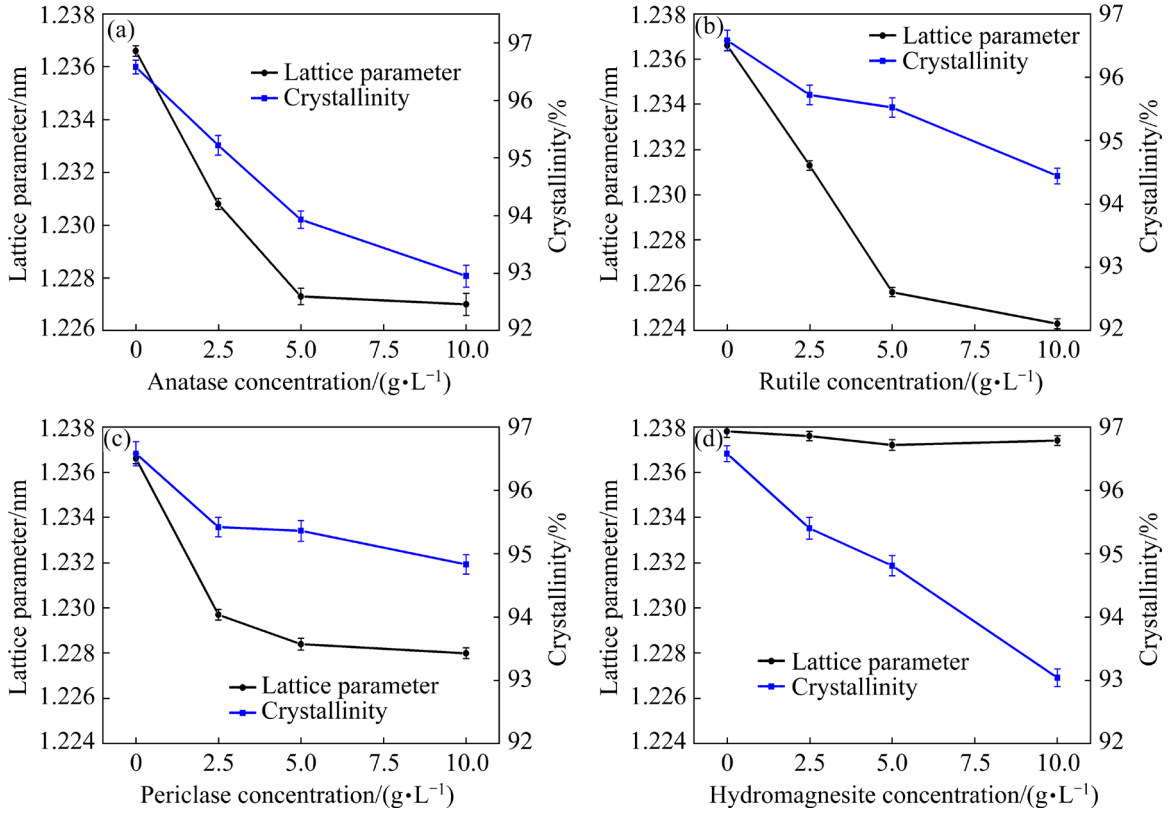

Fig. 4 Lattice parameters and crystallinity of HA with different Ti- and Mg-bearing minerals: (a) Anatase; (b) Rutile; (c) Periclase; (d) Hydromagnesite

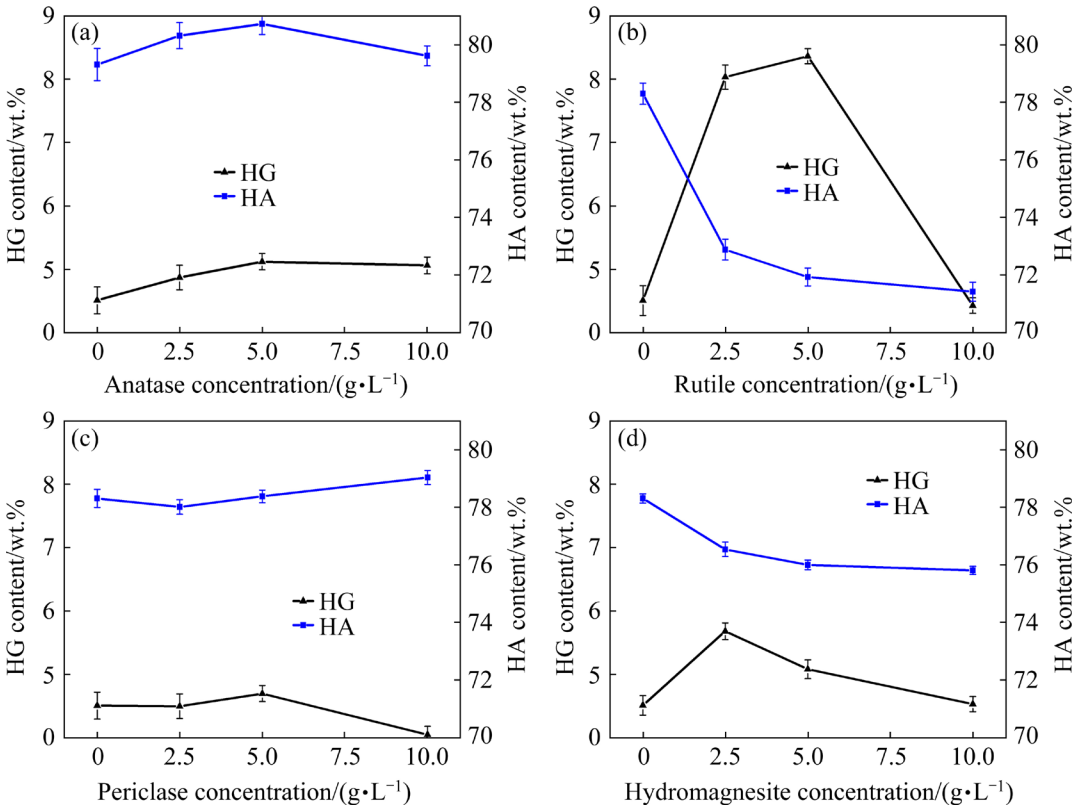

Fig. 5 Contents of HA and HG with different Ti- and Mg-bearing minerals: (a) Anatase; (b) Rutile; (c) Periclase; (d) Hydromagnesite

changes with the increase of anatase concentration, as given in Fig. 5(a). This indicates that the anatase cannot inhibit the HA formation, but alters its crystal structure. As shown in Fig. 5(b), the HA content notably decreases while the HG content substantially increases until the rutile concentration reaches 5 g/L. Hence, the rutile can inhibit the transformation from HG to HA in sodium aluminate solution. Excessive rutile reacts with CaO to form perovskite, slowing down the HG formation and affecting the substitution reaction of $Al(OH)_4^-$ by $Fe(OH)_4^-$ [24]. The contents of HG and HA change slightly with the increasing concentration of periclase as presented in Fig. 5(c). This is due to the more stable silicate structure formed by Ca^{2+} and $[SiO_4]^{4-}$ compared to the structure involving Mg^{2+} and $[SiO_4]^{4-}$. Mg^{2+} released by dissolving periclase cannot effectively substitute Ca^{2+} in HA and HG [25]. As seen from Fig. 5(d), the content of HG increases firstly and then decreases with the increasing concentration of hydromagnesite, which reaches the maximum when the hydromagnesite concentration is 2.5 g/L. Additionally, the HA content significantly reduces with an increasing concentration of hydromagnesite, indicating that the hydromagnesite hinders the HA formation in sodium aluminate solution.

3.2 Effect of Ti- and Mg-bearing minerals on microstructure

The microstructure of HA without Ti- and Mg-bearing minerals is given in Fig. 6, and the corresponding EDS results are illustrated in Table 1. Figures 6(a, b) reveal a relatively loose distribution of HA, predominantly forming agglomerates with spherical particles. Additionally, the crystallization of HA seems incomplete, evident in the formation of hollow pellets, as shown in Fig. 6(c). According to the EDS results, the molar ratios of Ca to Si and Al to Si (Point *A* in Fig. 6(c)) are 2.78 and 1.53, respectively, and the SiO_2 saturation coefficient (n) of HG ($3CaO{\cdot}Al_2O_3{\cdot}nSiO_2{\cdot}(6-2n)H_2O$) was calculated to be 1.25. In Fig. 6(d), the fully crystallized HA crystal exhibits a dense and smooth surface. The XRD patterns and EDS results indicate that, at Point *B* in Fig. 6(c), molar ratios of Ca to Si, Al to Si, and Fe to Si are 3.19, 1.04, and 1.48, respectively. The corresponding n value for HA ($3CaO{\cdot}(0.4Al_2O_3{\cdot}0.6Fe_2O_3){\cdot}nSiO_2{\cdot}(6-2n)H_2O$) is 0.9.

The SEM images of HA with 5 g/L Ti-bearing minerals are displayed in Fig. 7, and the corresponding EDS results are shown in Table 2. As viewed from Figs. 7(a–d), the HA particles have nearly spherical and flocculent structure and the particle size significantly becomes finer compared

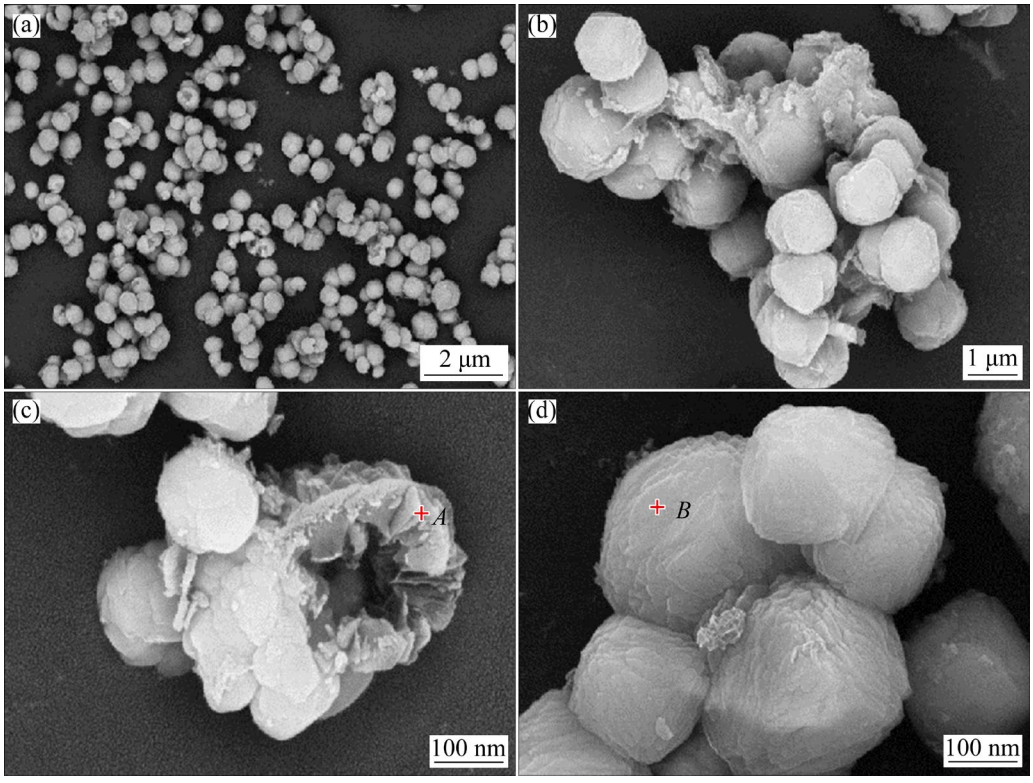

Fig. 6 SEM images of HA without Ti- and Mg-bearing minerals

Table 1 EDS results at different points corresponding to Fig. 6 (at.%)

Point	O	Na	Al	Si	Ca	Fe
A	67.78	0.84	8.76	5.74	15.96	1.92
B	73.41	0.64	4.03	3.87	12.35	5.71

with the HA without Ti- and Mg-bearing minerals, because of the dissolution and substitution of anatase in sodium aluminate solution. As per the EDS findings at Point *C* in Fig. 7(b), the elemental contents (molar fraction) of Ca, Al, Fe, Ti, and Si are 13.80%, 4.12%, 7.93%, 0.91%, and 6.03%, respectively. The corresponding molecular formula of HA with anatase calculated as $3CaO\cdot(0.45Al_2O_3\cdot 0.55Fe_2O_3)\cdot(0.2TiO_2\cdot 1.3SiO_2)\cdot 3H_2O$. The Fe/Si molar ratio was calculated to be 0.85 according to the molecular formula, while the Fe/Si molar ratio is 1.32 according to EDS. This disparity may stem from the re-precipitation of Fe_2O_3 dissolved in sodium aluminate solution. At Point *D* in Fig. 7(c), the molar ratios of Al to Ca, Fe to Ca, Ti to Ca, and Si to Ca are 0.16, 0.53, 0.05, and 0.45 respectively. This yields a molecular formula of HA with anatase as $3CaO\cdot(0.25Al_2O_3\cdot 0.75Fe_2O_3)\cdot(0.15TiO_2\cdot 1.35SiO_2)\cdot 3H_2O$.

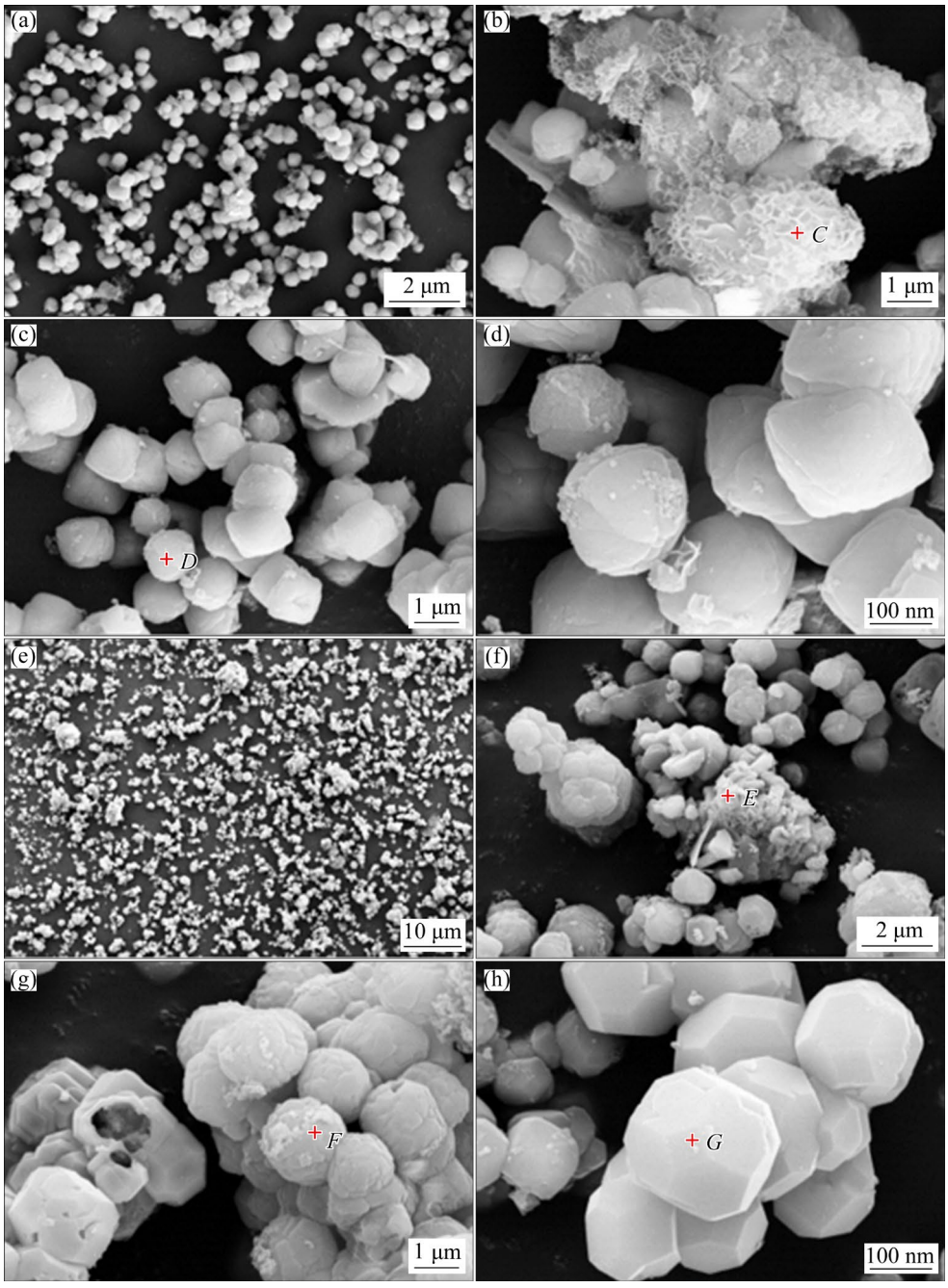

Fig. 7 SEM images of HA with 5 g/L anatase (a−d) and rutile (e, h)

Table 2 EDS results at different points corresponding to Fig. 7 (at.%)

Point	O	Na	Al	Si	Ca	Fe	Ti
C	67.21	−	4.12	6.03	13.80	7.93	0.91
D	64.09	−	2.59	7.43	16.45	8.65	0.80
E	57.12	−	−	0.35	0.56	41.58	0.38
F	64.18	1.43	3.04	6.59	14.98	8.44	1.33
G	70.75	−	1.86	2.87	12.37	7.52	4.64

As shown in Figs. 7(e−h), the HA with 5 g/L rutile is mainly agglomerated with spherical particles. The molar ratio of Fe to O is 0.73 (Point *E* in Fig. 7(f)), which is similar to the stoichiometric ratio of Fe_2O_3, indicating that the small particles attached to the surface of spherical particles are hematite. At Point *F* in Fig. 7(g), the molar ratios of Al to Ca, Fe to Ca, Ti to Ca, and Si to Ca are 0.20, 0.56, 0.09, and 0.44, respectively. The molecular formula of HA with rutile was derived as $3CaO\cdot(0.3Al_2O_3\cdot0.7Fe_2O_3)\cdot(0.27TiO_2\cdot1.33SiO_2)\cdot3H_2O$. Figure 7(h) illustrates the morphology of HA with 5 g/L rutile, primarily exhibiting agglomerated hexahedral particles. At Point *G* in Fig. 7(h), the molar ratios of Al to Ca, Fe to Ca, Ti to Ca, and Si to Ca are 0.15, 0.61, 0.38, and 0.23, respectively. The resulting molecular formula of HA with rutile is $3CaO\cdot(0.25Al_2O_3\cdot0.75Fe_2O_3)\cdot(1.15TiO_2\cdot0.65SiO_2)\cdot2.4H_2O$. Notably, the Ti^{4+}–Si^{4+} substitution degree in HA formed with rutile is higher than that with anatase, indicating rutile's increased incorporation into the HA crystal. The SiO_2 saturation coefficients of HA with Ti-bearing minerals are considerably lower than those without Ti-bearing minerals, indicating that higher concentrations of Ti-bearing minerals in sodium aluminate solution impede the desilication progress. Moreover, these findings highlight that the substantial substitution of Si^{4+} by Ti^{4+} significantly alters the HA morphology.

The microstructure of HA with 5 g/L Mg-bearing minerals is presented in Fig. 8. The HA is

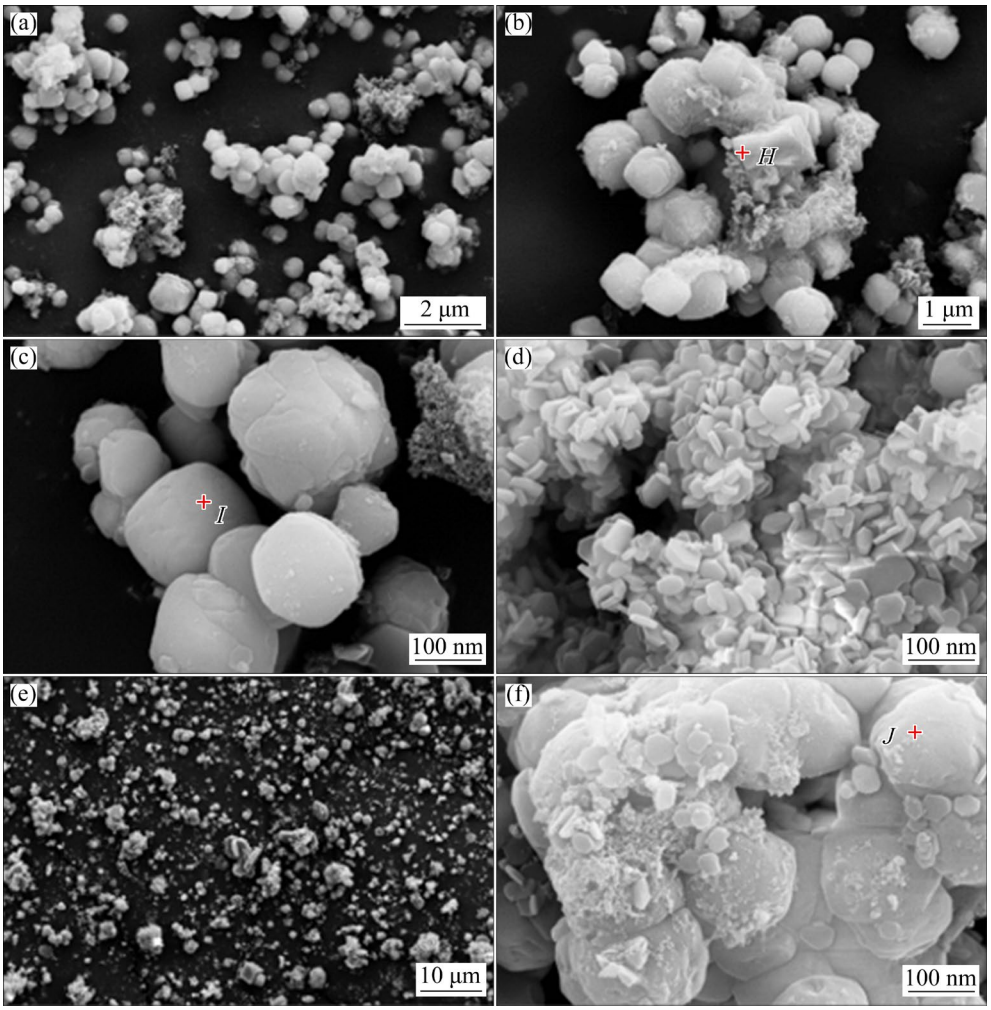

Fig. 8 SEM images of HA with 5 g/L periclase (a−d) and hydromagnesite (e, f)

predominantly formed by the aggregation of hexagonal plate particles, indicating that the growth direction of HA is changed by the existence of periclase in sodium aluminate solution (Figs. 8(a−d)). According to the EDS results in Table 3, the elemental composition indicates a Mg content of 15.31 at.% (Point *H* in Fig. 8(b)), identifying the regular hexagonal plate particles as $Mg(OH)_2$. At Point *I* in Fig. 8(c), the molar ratios of Ca to Si, Al to Si, Fe to Si, and Mg to Si are 2.41, 0.63, 1.20, and 0.12, respectively. The resulting molecular formula of HA with periclase is expressed as $(2.85CaO{\cdot}0.15MgO){\cdot}(0.35Al_2O_3{\cdot}0.65Fe_2O_3){\cdot}1.15SiO_2{\cdot}3.7H_2O$. Upon the comparison of Tables 1 and 2 with Table 3, distinct effects of periclase, anatase, and rutile on the mineral composition and element distribution of HA are evident. The crystal structure and the physical and chemical properties of HA are changed by Mg^{2+}−Ca^{2+} substitution. The reason is that the radius difference between Mg^{2+} and Ca^{2+} is large, and the ion substitution reaction changes the bond length and bond angle of HA [26−28].

Table 3 EDS results at different points in Fig. 8 (at.%)

Point	O	Al	Si	Ca	Fe	Mg
H	61.12	2.81	3.80	9.47	7.50	15.31
I	72.21	3.26	5.18	12.48	6.24	0.63
J	70.80	2.65	6.79	13.20	6.56	−

The morphology of HA with 5 g/L hydromagnesite appears relatively loose, mainly composed of fine particles (Figs. 8(e−f)). The EDS results at Point *J* in Fig. 8(f) reveal the contents (molar fraction) of O, Al, Si, Ca, and Fe atoms as 70.80%, 2.65%, 6.79%, 13.20%, and 6.56%, respectively. Additionally, the molar ratios of Ca to Si, Al to Si, and Fe to Si are calculated at 1.94, 0.39, and 0.97, respectively. The resulting molecular formula for HA with hydromagnesite is indicated as $3CaO{\cdot}(0.3Al_2O_3{\cdot}0.7Fe_2O_3){\cdot}1.55SiO_2{\cdot}2.9H_2O$. Remarkably, no detectable Mg element was found in HA, indicating that the dissolved Mg^{2+} in sodium aluminate solution does not integrate into the HA structure. This observation explains the slight alteration in HA's lattice parameters (from 1.236 to 1.238 nm) across different concentrations of hydromagnesite.

3.3 Effect of Ti- and Mg-bearing minerals on particle size

The PSD curves of the reaction products shift from a trimodal distribution to a four-peak distribution as the concentration of anatase increases, as shown in Fig. 9(a). The transition occurs when anatase concentration exceeds 5 g/L and is possibly caused by the aggregation of HA, HG, and calcium titanate. This shift in the PSD curves towards the left indicates a decrease in particle size of the reaction products, adversely affecting the settling of red mud. Furthermore, the average grain diameters of the reaction products progressively decrease with rising anatase concentrations, as shown in Fig. 9(b). Figure 9(c) illustrates the PSD curves exhibiting a clear trimodal distribution, which gradually shifts leftwards with increasing concentrations of rutile. It is evident that the presence of rutile leads to a reduction on the particle size of the reaction products (Fig. 9(d)), which is consistent with the presence of anatase. Additionally, in Fig. 9(e), the initial negative slope of the PSD curves and the widening distribution range with increasing periclase concentrations (from 2.5 to 10 g/L) suggest that the precipitation of magnesium hydroxide leads to particle aggregation. Consequently, the PSD curves of the reaction products shift rightwards, indicating an increase in particle size. As shown in Fig. 9(f), the average grain diameters of the reaction products increase significantly with the increasing concentration of periclase, which is in good agreement with the PSD curves in Fig. 9(e). With increasing hydromagnesite concentrations, the PSD curves shift from a trimodal distribution to a bimodal distribution and move rightwards (Fig. 9(g)). Unlike periclase, the slope of the PSD curves becomes smaller, indicating particle aggregation due to the formation of magnesium hydroxide and calcium carbonate in sodium aluminate solution. Compared with the data with periclase, the average grain diameters of the reaction products with hydromagnesite (Fig. 9(h)) are larger.

In Fig. 10, the specific surface area (SSA) of the reaction products shows a notable increase with higher concentrations of Ti-bearing minerals. As the concentration of Ti-bearing minerals exceeds 5 g/L, the SSA slows down significantly. Additionally, the SSA of the reaction products with rutile is significantly larger than that with anatase. Meanwhile, the SSA

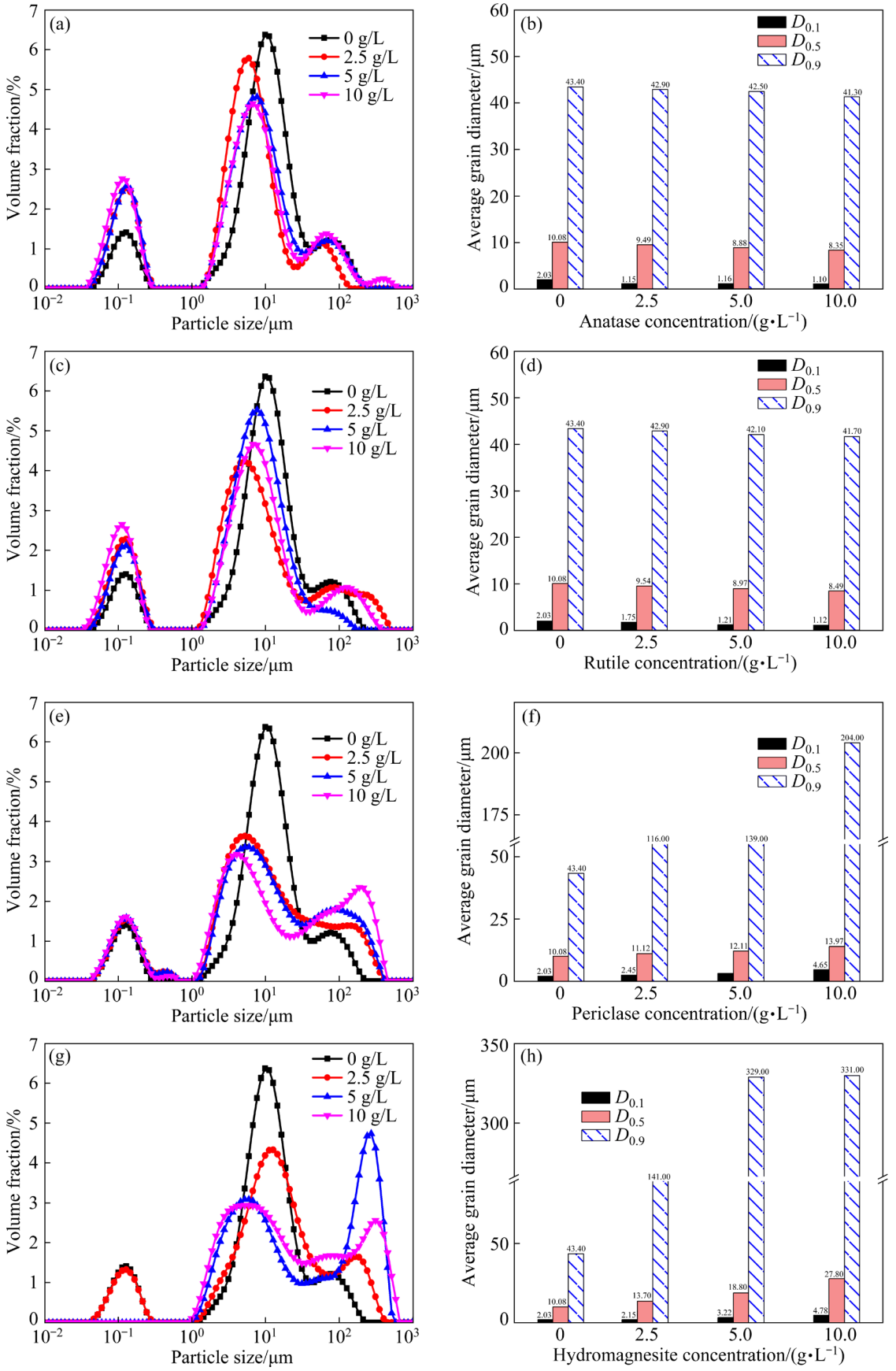

Fig. 9 PSD curves (a, c, e, g) and average grain diameters (b, d, f, h) of reaction products with different Ti- and Mg-bearing minerals: (a, b) Anatase; (c, d) Rutile; (e, f) Periclase; (g, h) Hydromagnesite

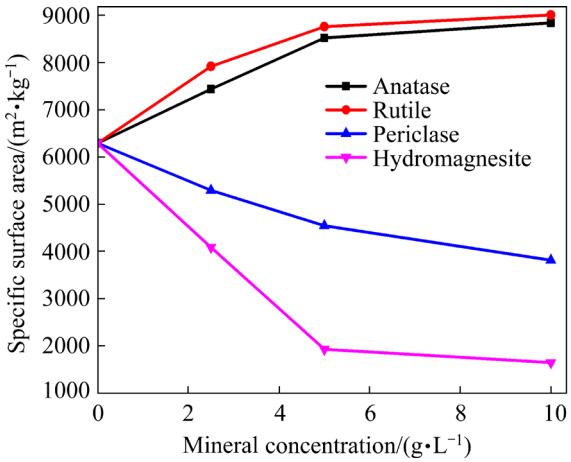

Fig. 10 Specific surface area of reaction products with different Ti- and Mg-bearing minerals

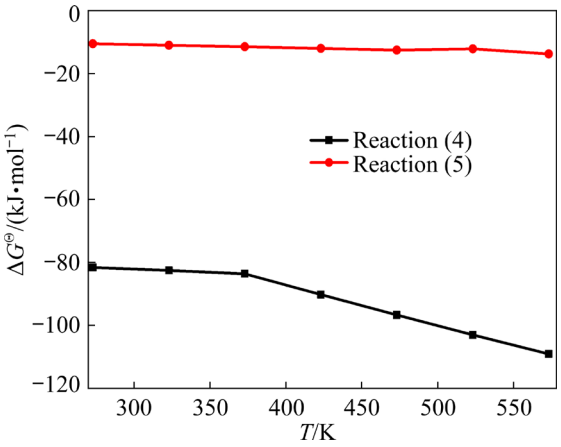

Fig. 11 Relationship between standard Gibbs free energy change ($\Delta G^{\ominus}$) and reaction temperature (T)

of the reaction products decreases gradually with the increasing concentration of Mg-bearing minerals, demonstrating that the increasing concentration of Mg-bearing minerals evidently increases the particle size of the reaction products. However, the reduction speed for SSA of HA slows down obviously when the concentration of Mg-bearing minerals exceeds 5 g/L.

3.4 Formation mechanism of HA with Ti- and Mg-bearing minerals

A series of intricate chemical reactions may occur during the formation of HA involving Ti- and Mg-bearing minerals in the Fe_2O_3–Na_2O–Al_2O_3–CaO–SiO_2–H_2O system, as outlined in Reactions (4) and (5). The corresponding standard Gibbs free energy changes were computed considering iron substitution coefficient (m), titanium and magnesium substitution coefficient (y), and silica saturation coefficient (x) set to 1, as depicted in Fig. 11. All standard Gibbs free energy changes are below zero, indicating that these substitution reactions can theoretically occur based on thermodynamics. Furthermore, these standard Gibbs free energy changes decrease as the reaction temperature increases. This illustrates that elevating the hydrothermal temperature promotes substitution reactions, particularly the Ti^{4+}–Si^{4+} ion substitution reaction. Notably, these thermodynamic calculations align well with the silicon index of sodium aluminate solution.

$$xyTi^{4+}+3CaO\cdot(Fe_2O_3)_m(Al_2O_3)_{1-m}\cdot xSiO_2\cdot(6-2x)H_2O=3CaO\cdot(Fe_2O_3)_m(Al_2O_3)_{1-m}\cdot x[(TiO_2)_y(SiO_2)_{1-y}]\cdot(6-2x)H_2O+xySi^{4+} \quad (4)$$

$$3yMg^{2+}+3CaO\cdot(Fe_2O_3)_m(Al_2O_3)_{1-m}\cdot xSiO_2\cdot(6-2x)H_2O=3[(MgO)_y(CaO)_{1-y}]\cdot(Fe_2O_3)_m(Al_2O_3)_{1-m}\cdot xSiO_2\cdot(6-2x)H_2O+3yCa^{2+} \quad (5)$$

Figure 12 illustrates the impact of Ti- and Mg-bearing minerals on the HA formation in sodium aluminate solution. The silicate crystal structure conforms to the *Ia3d* space group, where all cations are symmetrically fixed [29]. Typically, metal cations are distributed within the tetrahedral and octahedral interstices of the silicate crystal structure. In HA, the Si^{4+} coordinates with four neighboring O atoms to form a [SiO_4] tetrahedron, and the Fe^{3+} coordinates with six neighboring O atoms to form an [FeO_6] octahedron [30]. The framework of the HA structure consists of these [SiO_4] tetrahedra and [FeO_6] octahedra. Simultaneously, Ca^{2+} occupies the structural gaps and coordinates with eight neighboring O atoms to form a [CaO_8] dodecahedron. The Ti- and Mg-bearing minerals dissolved in sodium aluminate solution can occur Ti^{4+}–Si^{4+} and Mg^{2+}–Ca^{2+} ion substitution reactions in HA. The ionic radius of Mg^{2+} is smaller than that of Ca^{2+}, allowing for the Mg^{2+}–Ca^{2+} ion substitution. However, the chemical force of the Ca—Si bond surpasses that of the Mg—Si bond, leading to a larger energy requirement for Ca^{2+} diffusion compared to that of Mg^{2+} diffusion [25]. This disparity accounts for the relatively low degree of Mg^{2+}–Ca^{2+} substitution. Ti atom primarily exists as a substitution cation in the SiO_2 lattice, forming a Ti—O—Si bond in HA. Moreover, these ion substitution reactions increase the lattice distortion degree of HA, but decrease the lattice parameters

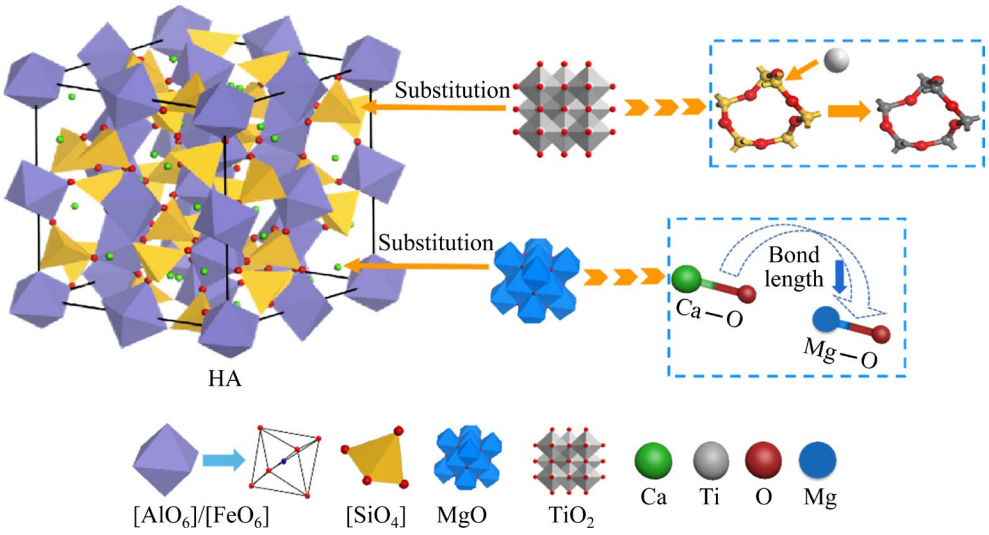

Fig. 12 Schematic diagram showing reaction mechanism of Ti- and Mg-bearing minerals on HA formation

and crystallinity. Consequently, the morphology of HA changes from spherical particles to flocculent structure and hexagonal plate particles.

4 Conclusions

(1) Anatase and rutile, when dissolved in sodium aluminate solution, are capable of substituting Si^{4+} in HA, with rutile exhibiting easier integration into HA compared to anatase. This Ti^{4+}–Si^{4+} substitution reaction results in decreased lattice parameters, reduced crystallinity, and smaller particle size of HA. Similarly, periclase, when dissolved, can substitute Ca^{2+} in HA, consequently decreasing the lattice parameters and crystallinity of HA. However, hydromagnesite, when dissolved, cannot enter into HA. Instead, the newly formed calcium carbonate contributes to an increase in the particle size of HA.

(2) The HA content shows minimal change with increasing concentrations of anatase and periclase. However, it decreases as the concentrations of rutile and hydromagnesite increase. Additionally, the SSA of HA increases with increasing concentrations of Ti-bearing minerals but decreases with rising concentrations of Mg-bearing minerals.

(3) The substitution reactions of Ti^{4+}–Si^{4+} and Mg^{2+}–Ca^{2+} considerably change the morphology of HA. HA manifests as a spherical and hexahedral structure with Ti-bearing minerals, whereas it forms as agglomerated hexagonal plates with Mg-bearing minerals.

CRediT authorship contribution statement

Hong-fei WU: Investigation, Data curation, Writing − Original draft; **Xiao-lin PAN:** Conceptualization, Supervision, Funding acquisition, Writing − Review & editing; **Ying-jie HE:** Investigation, Data curation; **Hai-yan YU:** Conceptualization.

Declaration of competing interest

The authors declare that they have no known competing financial interests or personal relationships that could have appeared to influence the work reported in this paper.

Acknowledgments

The authors greatly appreciate the financial supports from the National Key R&D Program of China (No. 2022YFC2904401), the National Natural Science Foundation of China (Nos. 22078055, 51774079), and the Fundamental Research Funds for the Central Universities, China (No. N2225002).

References

[1] BI Shi-wen, YU Hai-yan, YANG Yi-hong, ZHAO Fu-hui, YIN Zhong-lin, ZHAI Xiu-jing. Bayer process for the production of alumina [M]. Beijing: Metallurgical Industry Press, 2007. (in Chinese)

[2] ALDABERGENOVA S B, GHICOV A, ALBU S, MACAK J M, SCHMUKI P. Smooth titania nanotubes: Self-organization and stabilization of anatase phase [J]. Journal of Non-Crystalline Solids, 2008, 354 (19−25): 2190−2194.

[3] LI Xiao-bin, FU Wei-an, ZHOU Qiu-sheng, LIU Gui-hua, PENG Zhi-hong. Reaction behavior and mechanism of anatase in digestion process of diasporic bauxite [J]. Transactions of Nonferrous Metals Society of China, 2010, 20(1): 142−146.

[4] YIN Zhong-lin, GU Song-qing, BI Shi-wen. Reaction behavior of impurity minerals in bauxite slurry in preheating process condition of two stream process of diasporic bauxite in China [J]. The Chinese Journal of Nonferrous Metals, 2005, 15 (2): 310−315. (in Chinese)

[5] LIU Gui-hua, QI Tian-gui, TIAN Lü, ZHOU Qiu-sheng, PENG Zhi-hong, LI Xiao-bin. Reaction behavior of MgO in desilication process of sodium aluminate solution [J]. The Chinese Journal of Nonferrous Metals, 2013, 23(7): 2055−2060. (in Chinese)

[6] LI Xiao-bin, YU Shun-wen, LIU Nan, CHEN Yong-kun, QI Tian-gui, ZHOU Qiu-sheng, LIU Gui-hua, PENG Zhi-hong. Dissolution behavior of sodium titanate in sodium aluminate solutions at elevated temperatures [J]. Hydrometallurgy, 2014, 147: 73−78.

[7] BIAN Zhen-zhong, FENG Ya-li, LI Hao-ran. Extraction of valuable metals from Ti-bearing blast furnace slag using ammonium sulfate pressurized pyrolysis-acid leaching processes [J]. Transactions of Nonferrous Metals Society of China, 2020, 30: 2836−2847.

[8] DUDEK K, JONES F, RADOMIROVIC T, SMITH P. The effect of anatase, rutile and sodium titanate on the dissolution of boehmite and gibbsite at 90 °C [J]. International Journal of Mineral Processing, 2009, 93(2): 135−140.

[9] WHITTINGTON B I, CARDILE C M. The chemistry of tricalcium aluminate hexahydrate relating to the Bayer industry [J]. International Journal of Mineral Processing, 1996, 48(1/2): 21−38.

[10] WHITTINGTON B I. The chemistry of CaO and $Ca(OH)_2$ relating to the Bayer process [J]. Hydrometallurgy, 1996, 43(1): 13−35.

[11] YIN Zhong-lin, GU Song-qing. Influence of lime adding method on scaling process in Bayer preheating process of diasporic bauxite slurry [J]. The Chinese Journal of Nonferrous Metals, 2001, 11(5): 910−914. (in Chinese)

[12] PAN Xiao-lin, WU Hong-fei, LV Zhong-yang, YU Hai-yan, TU Gan-feng. Recovery of valuable metals from red mud: A comprehensive review [J]. Science of the Total Environment, 2023, 904: 166686.

[13] LI Xiao-bin, ZHOU Qiu-sheng, WANG Hao-yu, PENG Zhi-hong, LIU Gui-hua. Hydrothermal formation and conversion of calcium titanate species in the system Na_2O−Al_2O_3−CaO−TiO_2−H_2O [J]. Hydrometallurgy, 2010, 104(2): 156−161.

[14] LI Xiao-bin, YU Shun-wen, DONG Wen-bo, CHEN Yong-kun, QI Tian-gui, ZHOU Qiu-sheng, LIU Gui-hua, PENG Zhi-hong. Effect and mechanism of anatase on digestion performance of alumina [J]. Transactions of Nonferrous Metals Society of China, 2014, 24(11): 2864−2871.

[15] YIN Zhong-lin, BI Shi-wen, GU Song-qing. Study of reaction kinetics of Ti-containing minerals in preheating process of bauxite slurry [J]. Mining and Metallurgical Engineering, 2005, 25(4): 54−57. (in Chinese)

[16] CHESTER R, JONES F, LOAN M, OLIVEIRA A, RICHMOND W R. The dissolution behaviour of titanium oxide phases in synthetic Bayer liquors at 90 °C [J]. Hydrometallurgy, 2009, 96(3): 215−222.

[17] DUNCAN F N C, BRADT R C. Synthesis of magnesium aluminate spinels from bauxite and magnesia [J]. Journal of the American Ceramic Society, 2002, 85(12): 2995−3003.

[18] KUZNETSOVA N V, KUVYRKINA A M, SUSS A G, DAMASKIN A A, TSVETKOVA M V, POPKOVA L A, SHMIGIDIN Y I, PANOV A V. Effect of magnesium salts on the production of tcha and the feasibility of using the resulting compounds in the leaching of bauxites [J]. Metallurgist, 2008, 52(11): 616−624.

[19] YUAN Hua-jun, HUANG Fang, ZHAO Du. Study of scaling during autoclave digestion of Ping-guo Aluminum Plant—Phase composition and property (I) [J]. Light Metals, 2001(7): 12−16. (in Chinese)

[20] WU Yu-jun, DENG Dan-dan, JIANG Jun, LI Feng, ZENG Jia-qing, GUO Xu-yao, ZHU Feng, JIANG Yi-fan, XUE Sheng-guo. Ca-driven stable regulatory of alkalinity within desilication products: Experimental, modeling, transformation mechanism and DFT study [J]. Science of the Total Environment, 2023, 868: 161708.

[21] HONG Tao, LUO Jun, LIU Man-bo, ZHENG Shi-li, ZHANG Yi. Desilication of concentrated alkali solution by novel desilication reagent calcium hydroferrocarbonate: Part II. Desilication reaction and kinetics [J]. Hydrometallurgy, 2019, 184: 123−131.

[22] PAN Xiao-lin, WU Hong-fei, LIU Ji-long, LIU Qing-wen, YU Hai-yan. Hydrothermal formation mechanism of the efficient desilication product hydroandradite ($3CaO·Fe_2O_3·xSiO_2·(6−2x)H_2O$) [J]. Hydrometallurgy, 2021, 203: 105695.

[23] PAN Xiao-lin, WU Hong-fei, YU Hai-yan, BI Shi-wen. Precipitation of desilication products in CaO−Na_2O−Al_2O_3−SiO_2−H_2O system based on the Bayer process [J]. Hydrometallurgy, 2020, 197: 105469.

[24] XU B A, SIMITH P. The effect of iron sources on caustic and alumina recovery from synthetic Bayer DSP (sodalite) [J]. Hydrometallurgy, 2012, 129: 26−29.

[25] DU W, CLARK S M, WALKER D. Thermo-compression of pyrope−grossular garnet solid solutions: Non-linear compositional dependence [J]. American Mineralogist, 2015, 100: 215−222.

[26] BOFFA B T, CARPENTER M A, GEIGER C A, KOZIAL A M. Local structural heterogeneity in garnet solid solutions [J]. Physics and Chemistry of Minerals, 1999, 26: 554−569.

[27] ZHANG Ren, ZHENG Shi-li, MA Shu-hua, ZHANG Yi. Recovery of alumina and alkali in Bayer red mud by the formation of andradite−grossular hydrogarnet in hydrothermal process [J]. Journal of Hazardous Materials, 2011, 189: 827−835.

[28] DU Wei, HAN Bao-fu, CLARK S M, WANG Yi-chuan, LIU Xi. Raman spectroscopic study of synthetic pyrope−grossular garnets: Structural implications [J]. Physics and Chemistry of Minerals, 2018, 45: 197−209.

[29] DILNESA B Z, LOTHENBACH B, RENAUDIN G, WICHSER A, KULIK D. Synthesis and characterization of hydrogarnet $Ca_3(Al_xFe_{1-x})_2(SiO_4)_y(OH)_{4(3-y)}$ [J]. Cement and Concrete Research, 2014, 59: 96−111.

[30] WU Hong-fei, PAN Xiao-lin, ZHU Mi-mi, YU Hai-yan. Structural stability and electronic properties of complex silicate compound of hydroandradite [J]. Materials Today Communications, 2023, 36: 106878.

含钛、镁矿物对钙铁榴石水热形成的影响

吴鸿飞[1,2,3]，潘晓林[1,2,3]，何英杰[2]，于海燕[1,2,3]

1. 东北大学 多金属共生矿生态化冶金教育部重点实验室，沈阳 110819；
2. 东北大学 冶金学院，沈阳 110819；
3. 沈阳市有色金属资源循环利用重点实验室，沈阳 110819

摘　要：采用 X 射线衍射仪、扫描电镜和粒度分析仪研究在合成铝酸钠溶液水热转化过程中含钛、镁矿物对高效脱硅产物钙铁榴石晶体结构、微观形貌、粒度分布和形成机理的影响。结果表明，溶解在铝酸钠溶液中的锐钛矿、金红石和方镁石在钙铁榴石生成过程中分别发生 Ti^{4+}−Si^{4+}和 Mg^{2+}−Ca^{2+}离子取代反应，而溶解在铝酸钠溶液中的水菱镁石则不能进入钙铁榴石。钙铁榴石的含量随锐钛矿和方镁石含量的增加变化很小，而其含量随金红石和水菱镁石含量的增加大幅降低。含钛矿物使钙铁榴石的粒度减小、比表面积增大，而含镁矿物的影响正好相反。含钛、镁矿物的存在使钙铁榴石的微观形貌由球形颗粒转变为絮状结构和六方板状颗粒。

关键词：钙铁榴石；锐钛矿；金红石；方镁石；水菱镁石；脱硅；水热转化

(Edited by Wei-ping CHEN)